Molecular Cell
Article

Molecular Imprinting as a Signal-Activation Mechanism of the Viral RNA Sensor RIG-I

Bin Wu,[1,3] Alys Peisley,[1,3] David Tetrault,[4] Zongli Li,[2,6] Edward H. Egelman,[5] Katharine E. Magor,[4] Thomas Walz,[2,6] Pawel A. Penczek,[7] and Sun Hur[1,3,*]
[1]Department of Biological Chemistry and Molecular Pharmacology
[2]Department of Cell Biology
Harvard Medical School, Boston, MA 02115, USA
[3]Program in Cellular and Molecular Medicine, Children's Hospital Boston, Boston, MA 02115, USA
[4]Department of Biological Sciences and the Li Ka Shing Institute of Virology, University of Alberta, Edmonton, AB T6G 2E9, Canada
[5]Department of Biochemistry and Molecular Genetics, University of Virginia, Charlottesville, VA 22908, USA
[6]Howard Hughes Medical Institute, Chevy Chase, MD 20815, USA
[7]Department of Biochemistry and Molecular Biology, The University of Texas-Houston Medical School, Houston, TX 77030, USA
*Correspondence: sun.hur@childrens.harvard.edu
http://dx.doi.org/10.1016/j.molcel.2014.06.010

SUMMARY

RIG-I activates interferon signaling pathways by promoting filament formation of the adaptor molecule, MAVS. Assembly of the MAVS filament is mediated by its CARD domain ($CARD^{MAVS}$), and requires its interaction with the tandem CARDs of RIG-I ($2CARD^{RIG-I}$). However, the precise nature of the interaction between $2CARD^{RIG-I}$ and $CARD^{MAVS}$, and how this interaction leads to $CARD^{MAVS}$ filament assembly, has been unclear. Here we report a 3.6 Å electron microscopy structure of the $CARD^{MAVS}$ filament and a 3.4 Å crystal structure of the $2CARD^{RIG-I}$:$CARD^{MAVS}$ complex, representing $2CARD^{RIG-I}$ "caught in the act" of nucleating the $CARD^{MAVS}$ filament. These structures, together with functional analyses, show that $2CARD^{RIG-I}$ acts as a template for the $CARD^{MAVS}$ filament assembly, by forming a helical tetrameric structure and recruiting $CARD^{MAVS}$ along its helical trajectory. Our work thus reveals that signal activation by RIG-I occurs by imprinting its helical assembly architecture on MAVS, a previously uncharacterized mechanism of signal transmission.

INTRODUCTION

RIG-I and MDA5 represent a conserved family of the vertebrate innate immune receptors that detect viral RNAs at the early stage of infection and elicit the antiviral immune response by transcriptional upregulation of type I interferons (IFNs) (Pichlmair and Reis e Sousa, 2007; Takeuchi and Akira, 2009). RIG-I and MDA5 are expressed by a wide range of tissues and are functional in the cytoplasm. They also share the same domain architecture, consisting of an N-terminal tandem caspase activation recruitment domain (2CARD) that is responsible for signal activation, and a central DExD/H motif helicase domain and C-terminal domain (CTD), which together function as an RNA recognition unit (Yoneyama and Fujita, 2008). Despite the shared domain architecture and the common downstream signaling pathways, RIG-I and MDA5 play nonredundant roles by recognizing largely distinct groups of viruses through distinct RNA specificity (Kato et al., 2011; Wilkins and Gale, 2010).

Structural and biochemical analysis of RIG-I and MDA5, from our laboratory and others, have revealed how these receptors utilize the common domain architecture to recognize distinct groups of viral RNAs (Jiang et al., 2011; Kowalinski et al., 2011; Luo et al., 2011; Wu et al., 2013). We have shown that while RIG-I binds to double-stranded RNA (dsRNA) ends as a monomer in the absence of ATP, it forms short filamentous oligomers near a dsRNA end during ATP hydrolysis (Peisley et al., 2013). This oligomer assembly allows clustering of 2CARD for its own oligomerization and, at the same time, enables recognition of viral signatures at dsRNA ends (such as 5′-triphosphate) as well as the overall dsRNA length (Patel et al., 2013; Peisley et al., 2013). By contrast, MDA5 binds to dsRNA in a highly cooperative manner, forming long filaments on dsRNA in the absence of ATP (Berke et al., 2012; Peisley et al., 2011; Wu et al., 2013). ATP hydrolysis, however, triggers rapid filament-end disassembly, which enables MDA5 to regulate its filament stability and the signaling activity according to the length of dsRNA over a wide range (Kato et al., 2008; Peisley et al., 2012).

In stark contrast to the detailed understanding of how RIG-I and MDA5 recognize viral RNAs, the molecular mechanisms by which these receptors activate antiviral signaling pathways, and how they interact with the downstream adaptor molecule, MAVS, have been poorly understood. In the absence of viral infection, 2CARD of RIG-I (and possibly MDA5) is in the autosuppressed state by forming an intramolecular interaction with the helicase domain (Kowalinski et al., 2011). This interaction is presumably released upon RNA binding as 2CARD competes with RNA for the same binding site in the helicase domain (Kowalinski et al., 2011). The released 2CARD of RIG-I ($2CARD^{RIG-I}$) then forms a homotetramer when brought into proximity upon RIG-I filament formation (Peisley et al., 2013) and/or upon binding to

K63-linked polyubiquitin chains (K63-Ub_n) (Jiang et al., 2012). Our recent crystal structure of $2CARD^{RIG-I}$ in complex with K63-Ub_2 revealed a core tetrameric structure of $2CARD^{RIG-I}$ encircled and stabilized by K63-Ub_2, explaining how K63-Ub_n promotes 2CARD tetramerization (Peisley et al., 2014). The $2CARD^{RIG-I}$ tetramer then interacts with the N terminus of MAVS containing a single copy of CARD ($CARD^{MAVS}$), and stimulates formation of self-perpetuating filaments of $CARD^{MAVS}$ on mitochondria (Hou et al., 2011). MAVS filament, in turn, activates the IFNα/β signaling pathway by recruiting further downstream signaling molecules, such as TRAF2, TRAF5, and TRAF6 (Liu et al., 2013). The importance of MAVS filament formation in its cellular function has been further demonstrated by a strong correlation between filament formation in vitro and signaling activity in cells (Peisley et al., 2014; Peisley et al., 2013), as well as the sufficiency of $CARD^{MAVS}$ filament seed to induce filament formation by full-length MAVS and subsequent activation of downstream signaling pathways (Hou et al., 2011).

MAVS filament nucleation by RIG-I and MDA5 thus represents the first intermolecular signal propagation event in the signaling pathway of these receptors. A few models have been proposed to explain how RIG-I and MDA5 trigger MAVS filament nucleation (Berke et al., 2013; Peisley et al., 2014; Rawling and Pyle, 2014; Xu et al., 2014), but the challenge commonly associated with structural investigation of the nucleator:filament interaction has thus far prevented mechanistic understanding of this key signal transduction event. Here, we report our 3.6 Å electron microscopy (EM) structure of the $CARD^{MAVS}$ filament and 3.4 Å crystal structure of the $2CARD^{RIG-I}$:$CARD^{MAVS}$ complex obtained through a protein-engineering approach. Our $CARD^{MAVS}$ filament structure is vastly different from a recently published 9.6 Å model of the $CARD^{MAVS}$ filament (Xu et al., 2014). Our structures, together with functional analyses, reveal the mechanism by which RIG-I activates MAVS.

RESULTS

EM Reconstruction of the $CARD^{MAVS}$ Filament

$CARD^{MAVS}$ is both necessary and sufficient to form the MAVS filament (Hou et al., 2011). To understand the structural organization of the $CARD^{MAVS}$ filament, we first generated filaments using isolated $CARD^{MAVS}$ with 19 additional amino acids (aa) at the N terminus and the P2A mutation (Figures 1A and S1A available online). This modification improved solubility of the $CARD^{MAVS}$ filament without affecting the cellular signaling activity in full-length MAVS (Figure S1B). The average power spectrum of the 31.7-nm-long overlapping filament segments indicated that the $CARD^{MAVS}$ filament exhibits a helical symmetry of a twist angle of 101.1° and an axial rise of 5.13 Å (Figure S1D). Using these parameters and a helical geometrically constrained reconstruction approach (see Supplemental Experimental Procedures), we reconstructed the electron density map of the $CARD^{MAVS}$ filament (Figure 1B). The final map has an overall resolution of 3.6 Å based on the Fourier shell correlation (FSC) = 0.5 criterion (Figure S1E).

We first performed rigid-body docking of monomeric $CARD^{MAVS}$ (Potter et al., 2008) to the reconstructed EM map, followed by structural refinement of individual side chains using a crystallographic refinement program (Table 1). High resolution of the density map not only enabled unambiguous identification of the orientation of individual CARDs within the filament, but also correctly predicted many of the bulky side chains (Figure 1B). The final model after refinement showed a nearly identical conformation as the monomeric $CARD^{MAVS}$ (Figure 1C), suggesting that the filament is formed through rigid-body assembly. Cross-beta structure commonly observed in amyloid fibers was absent, consistent with the previous report that the MAVS filament is not stained with Congo red (Hou et al., 2011).

Each $CARD^{MAVS}$ interacts with its six nearest neighbors using six distinct surface areas (Ia/b, IIa/b, and IIIa/b) forming three types of intermolecular interactions (Ia:Ib, IIa:IIb, and IIIa:IIIb) (Figure 1D). These interactions resemble those previously identified from the $2CARD^{RIG-I}$ tetramer (Peisley et al., 2014) and oligomers of other death domains (DDs) (Ferrao and Wu, 2012). Each $CARD^{MAVS}$ interacts with the neighboring units in the identical manner regardless of its position within the filament. Thus, the $CARD^{MAVS}$ filament is best described as a single-stranded left-handed helix (Figure 1D), in which IIIa:IIIb constitutes the intrastrand interaction, whereas Ia:Ib and IIa:IIb form the interstrand interactions (Figures S1F and S1E). Although detailed nature of some of these interactions could not be clearly defined due to limited resolution of the map, survey of residues at the interface indicates that inter-CARD interactions are mediated by a combination of electrostatic and hydrophobic interactions (Figure 1E).

Interestingly, our previous crystal structure of the $2CARD^{RIG-I}$ tetramer also displayed a single-stranded left-handed helical arrangement with similar twist and rise values (Peisley et al., 2014). In this structure, the first and second CARDs of $2CARD^{RIG-I}$ are tightly joined together through the IIa:IIb interaction, and the resultant 2CARDs are stacked together in a way that the first helical turn of the first CARD is extended by the second helical turn of the second CARD (Figure 1F). To compare the helical assembly of the $CARD^{MAVS}$ filament and the $2CARD^{RIG-I}$ tetramer, we superposed the two helical turns of the $CARD^{MAVS}$ filament onto the $2CARD^{RIG-I}$ tetramer structure (Figure 1F). The two structures aligned with remarkable agreement, suggesting that the two assembly structures share the same helical geometry. This observation prompted us to hypothesize that the $2CARD^{RIG-I}$ tetramer triggers the $CARD^{MAVS}$ filament formation by serving as a helical template (to be discussed further in Figure 3).

Charge-Complementary Mutations Support the $CARD^{MAVS}$ Filament Structure

One way to test the functionality of the MAVS filament model is to examine the effect of mutations in the interface on filament formation in vitro and signaling activity in cells. Surface residues involved in each of the interactions revealed in our structure closely matched those previously identified to be important in our screens and others (Peisley et al., 2013, 2014; Xu et al., 2014) (Table S1). However, the large surface areas involved in the interface make such a loss-of-function mutation analysis insufficient to validate the structure (Egelman, 2010). In fact, the same loss-of-function mutation data in Table S1 are consistent with both our filament structure and the one recently proposed (Xu et al., 2014). Note that the latter differs significantly

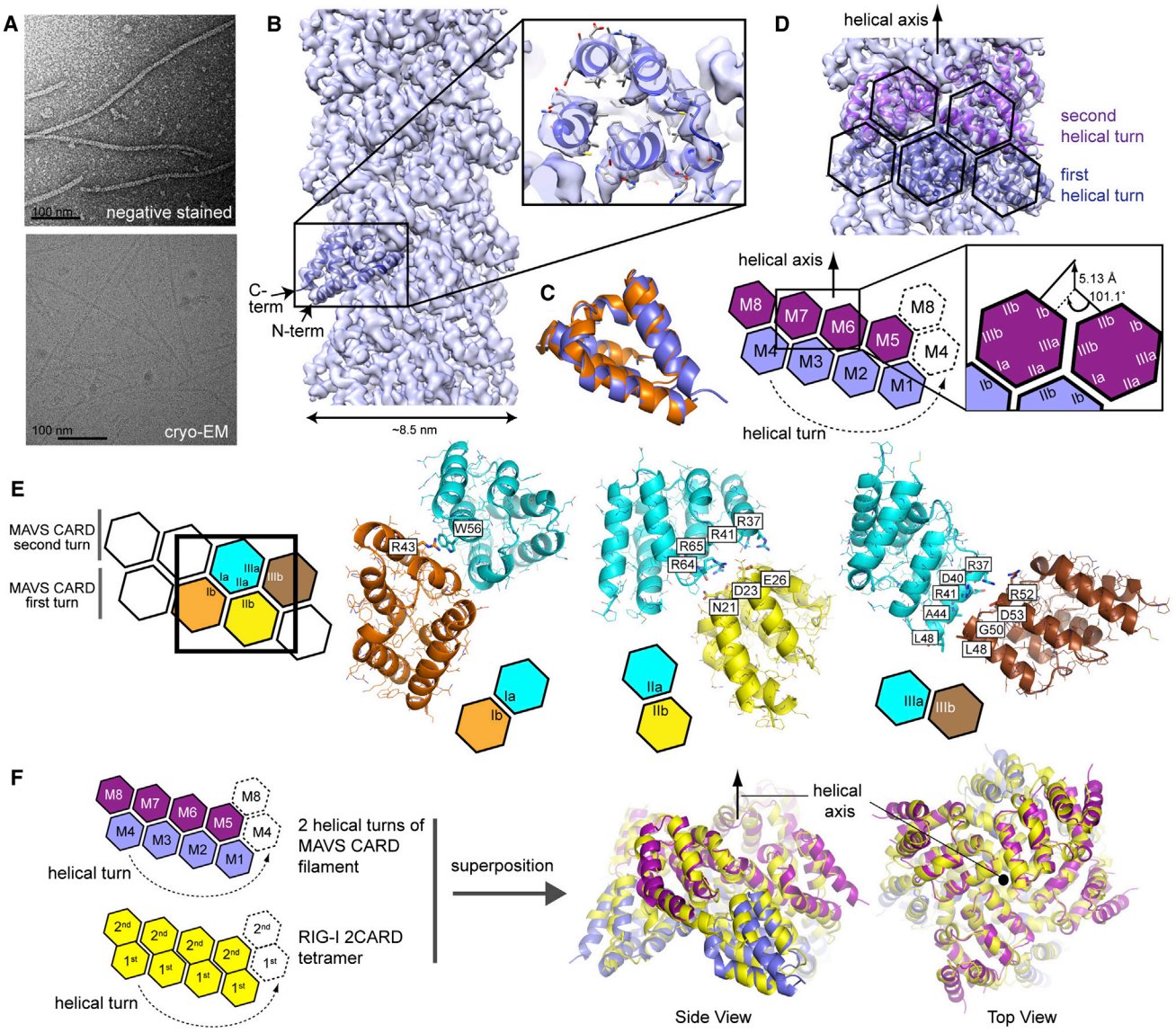

Figure 1. MAVS CARD Forms a Left-Handed Single-Stranded Filament Using a Common Helical Symmetry Shared with the RIG-I 2CARD Tetramer

(A) Representative electron micrographs of negatively stained and cryo-CARD^{MAVS} filaments.

(B) Reconstructed EM density map of the CARD^{MAVS} filament and monomeric CARD^{MAVS} (PDB 2VGQ) docked into the map (using the program Chimera). The N and C termini (residues 1 and 97) face the periphery of the filament and are indicated by arrows. The density for the 19 aa extension at the N terminus was unresolved, suggesting its flexibility.

(C) Superposition of the structures of CARD^{MAVS} before refinement (PDB 2VGQ, orange) and after refinement (slate).

(D) A model of the CARD^{MAVS} filament, showing two helical turns. Shown below is the 2D representation of the helical assembly. The CARD^{MAVS} filament displays a left-handed single-stranded structure with a twist angle of 101.1° and a rise of 5.13 Å. Each CARD^{MAVS} interacts with its six nearest neighbors: two neighbors along the helical trajectory through the IIIa:IIIb interaction (intrastrand interaction), and two neighbors each through the Ia:Ib and IIa:IIb interactions between adjacent helical turns (interstrand interaction). See also Figure S1F.

(E) Details of the Ia:Ib, IIa:IIb, and IIIa:IIIb interactions. Residues at the interface are shown in stick models. Color code was chosen to simplify the comparison with Figure 5A.

(F) Superposition of the two helical turns of the CARD^{MAVS} filament from (D) and the helical tetramer of 2CARD^{RIG-I} (PDB 4NQK).

from our structure in both overall architecture (left-handed, three-stranded) as well as local inter-CARD interactions (Figure S2B). Considering the similarity between the power spectra of our filaments and those of Xu et al., this large discrepancy in the final models most likely arose from the use of incorrect helical symmetry in their reconstruction, rather than the intrinsic difference in the filament samples. The validity of our helical symmetry can be seen at higher resolution by the visualization of the protein

Table 1. Refinement Statistics of the CARD^{MAVS} Filament

Statistics for CARD^{MAVS} Filament Model and Pseudocrystallographic Refinement	
Cell dimensions[a]	
a, *b*, *c* (Å)	105.6, 105.6, 88.0
α, β, γ (°)	90.0, 90.0, 90.0
Resolution (Å)	99–3.64
No. reflections	33,916 (2,900)
R_{work}[b]	23.8%
R_{free}[c]	27.6%
No. of protein atoms	6,344
Average *B* factors	136.08
Rmsd	
Bond lengths (Å)	0.007
Bond angles (°)	1.257
Dihedral angle (°)	14.668
Ramachandran plot	
Outliers	1.2%
Allowed	98.8%
Favored	95.0%

[a]Arbitrary cell dimensions were chosen to cover the two helical turns of the CARD^{MAVS} filament.
[b]$R = \sum_h ||F(h)_{obs}| - |F(h)_{calc}|| / \sum_h |F(h)_{obs}|$.
[c]R_{free} was calculated for 5.1% of reflections randomly excluded from the refinement.

α-helical secondary structure with correct handedness, which is absent in the reconstruction by Xu et al.

For more rigorous validation of our structural model, we employed a charge-complementary mutagenesis approach, where filament formation was monitored upon mutation of either one or both of the interacting residues into complementary aa. We chose to investigate W56 and R43 in the Ia/Ib interface, as these residues were identified to be important from both our functional assays and those of Xu et al. (Table S1), and the Ia/Ib interface is simpler than IIa/IIb and IIIa/IIIb, with a clear density map supporting a direct interaction between W56 and R43 (Figure 2A). Finally, unlike our structure, W56 and R43 are far apart in Xu et al. (Figure S2B), further providing an opportunity to distinguish between our model and that of Xu et al.

In our previous mutagenesis analyses of MAVS (Peisley et al., 2013, 2014), the intrinsic ability of CARD^{MAVS} to form filaments in vitro and *E. coli* showed a strong correlation with signaling activity in human 293T cells (Table S1). In these experiments, we have used CARD^{MAVS} fused to a fluorescent tag, SNAP (CARD^{MAVS}-S), which enables us to monitor its filament formation and extension by native gels as well as EM. As expected, single point mutations, W56R, R43D, and R43E, completely abrogated filament formation by CARD^{MAVS}-S (Figures 2B and 2C). However, the double mutations W56R/R43D and W56R/R43E restored the filament-formation activity of CARD^{MAVS}-S, albeit at lower efficiency than wild-type (Figure 2B). While the W56R/R43D and W56R/R43E filaments showed a similar thickness as the wild-type filament, they were significantly longer, which likely reflects less efficient nucleation of the mutant filaments, consistent with the smaller number of filaments. While filaments of wild-type and the double-mutant CARD^{MAVS}-S can be rapidly extended by the monomer of the same type, they could not cross-seed each other (Figure 2D), consistent with the notion that the charge complementarity between residues 56 and 43 is required for filament formation. Together, these results suggest that W56 and R43 form a direct interaction within the MAVS filament, which is consistent with our MAVS filament model, but not that of Xu et al.

Analysis of CARD^{MAVS}-S from duck showed that they also form filaments (Figure S2E), suggesting that filament formation is a feature of MAVS that is conserved across species. Sequence alignment showed, however, that residues at the inter-CARD interface, in particular W56 and R43, in human, are poorly conserved in duck (Figure S2A). Despite the lack of conservation, mutations of Y56 or H43 in duck MAVS, which correspond to W56 and R43 in human MAVS, abrogated its filament formation in vitro and IFNβ signaling in chicken fibroblast cell line, DF-1 (Figures S2E and S2F). The charge-complementary mutations of Y56R and H43E partially restored its ability to form filaments (Figure S2E). Although the double-mutant filaments appeared more curvy than the wild-type, likely reflecting less optimal surface compatibility of the mutant, the complete abrogation of filament formation by either of the single mutations and rescue of filament formation by the double mutation supports the notion that residues 56 and 43 interact with each other in duck MAVS filament, as well as in human MAVS filament.

Protein Engineering Strategies for Crystallization of the 2CARD^{RIG-I}:CARD^{MAVS} Complex

To understand precisely how the 2CARD^{RIG-I} tetramer initiates the CARD^{MAVS} filament formation, we developed strategies to crystallize the 2CARD^{RIG-I} and CARD^{MAVS} complex. As crystallization of polymerizing proteins, such as CARD^{MAVS}, is challenging, we employed a series of protein engineering approaches, which led to identification of the fusion construct (Figure 3A) that formed a homogeneous tetramer (Figure 3B) and produced well-diffracting crystals.

From our initial screens of multiple surface mutants of both 2CARD^{RIG-I} and CARD^{MAVS}, we identified two candidate mutants: E52A in 2CARD^{RIG-I} and D23K/E26K/E80K (KKK) in CARD^{MAVS}. E52A resides on the bottom surface of the 2CARD tetramer (surface IIa of the first CARD, Figure 3A) and improved solubility and the tetramer stability without interfering with IFN signaling in cells (Figures S3A and S3B). The KKK residues, on the other hand, reside on the top surface of the filament (surface IIb, Figure 3A), and are involved only in the vertical interstrand interaction, not in formation of the single helical turn. Accordingly, the KKK mutant of CARD^{MAVS} did not form long filaments, but formed oligomers of heterogeneous size (Figure S3C). MAVS with the KKK mutation retained a moderate level of signaling activity in cells (Figure S3A), suggesting that the small oligomeric structure formed by the mutant likely recapitulates the functional form of the CARD^{MAVS} filament.

We hypothesized that fusion of CARD^{MAVS} to 2CARD^{RIG-I} would restrict the stoichiometry of the 2CARD:CARD interaction to a 1:1 molar ratio, and would prevent oligomerization of CARD^{MAVS} beyond a tetramer. The covalent fusion of the

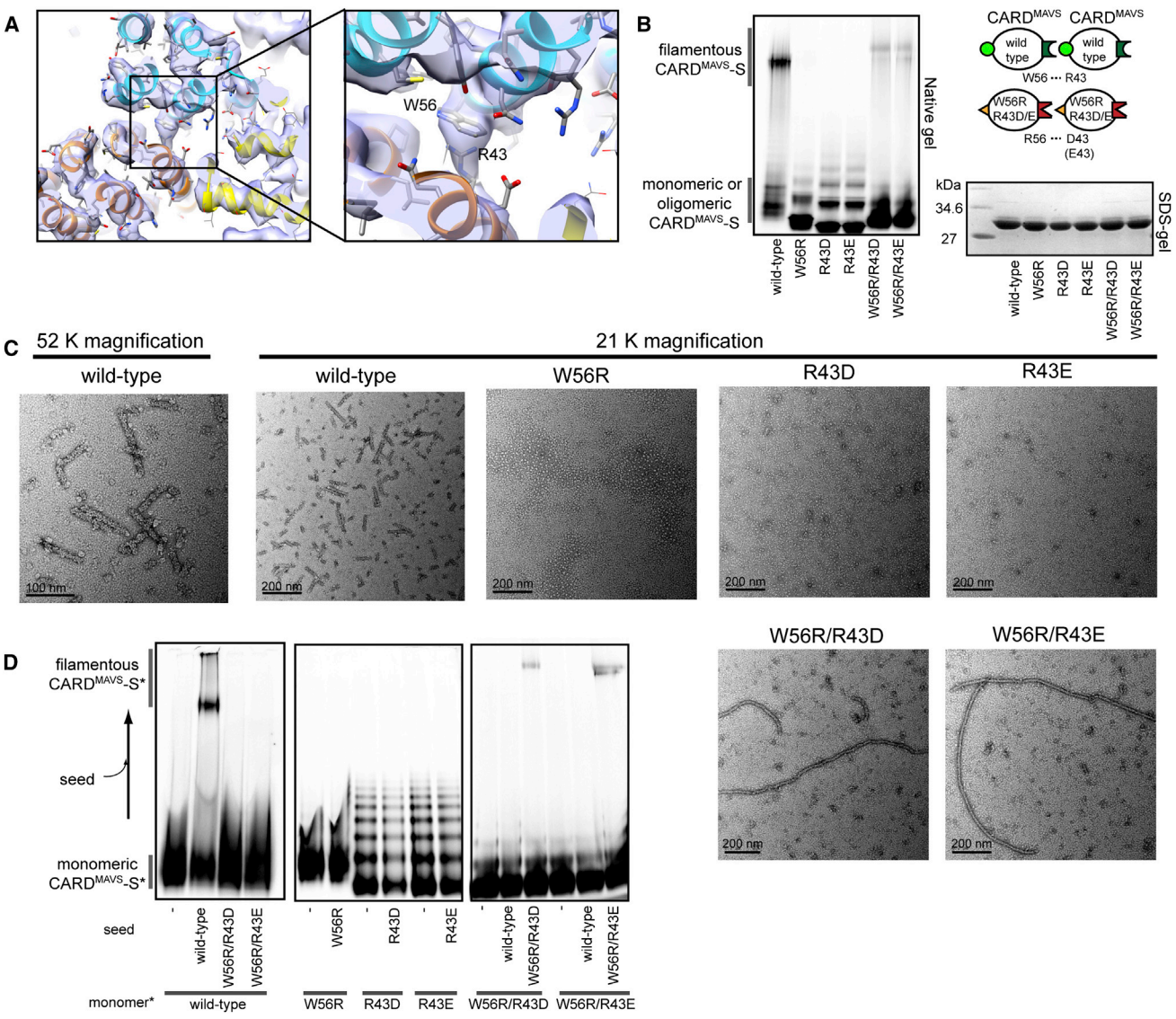

Figure 2. Charge-Complementary Mutagenesis Supports the CARD^{MAVS} Filament Reconstruction

(A) The CARD^{MAVS} filament model and the EM map, showing the inter-CARD^{MAVS} interface. See Figure 1E for the color code. Shown on the right is the magnified view of the type I interface, unambiguously showing that W56 and R43 form a direct contact, likely involving a pi:cation interaction.

(B) Effect of charge-complementary mutations on filament formation of CARD^{MAVS}, as measured by native gel analysis. CARD^{MAVS} was fused to a fluorescent tag, SNAP (CARD^{MAVS}-S), which was conjugated with Alexa 647 for gel imaging. Shown on the right are pictorial diagrams that illustrate the effect of charge-complementary mutations. See also Figures S2C and S2D.

(C) EM images of the samples in (B). Wild-type CARD^{MAVS} filaments are shown at 52,000 and 21,000 magnifications for clear visualization of the filamentous structure.

(D) Filament seeding assays to test the cross-reactivity between wild-type and the double mutants W56R/R43D and W56R/R43E. Monomeric CARD^{MAVS}-S was prepared by either refolding of the filament (for wild-type) or fractionation by size exclusion chromatography (SEC). Purified monomer was fluorescently labeled using Alexa 647, and mixed with unlabeled seed filaments (sample from B) at a monomer-to-seed mass ratio of 20:1.

two would also stabilize the 2CARD:CARD interaction, whose transient nature has thus far prohibited its detailed biochemical analysis. Consistent with our prediction, the 2CARD$^{RIG\text{-}I(E52A)}$-CARD$^{MAVS(KKK)}$ fusion protein formed a tetramer, but not larger oligomers, and shortening of the linker between 2CARD$^{RIG\text{-}I}$ and CARD^{MAVS} from 42 to 16 aa, further promoted its tetramerization (Figure 3B). Unlike isolated 2CARD$^{RIG\text{-}I}$ (Figure S3B), the tetramer formation of the fusion protein did not require K63-Ub$_n$. Instead, it depended on the intact surface III of CARD^{MAVS}, as well as 2CARD$^{RIG\text{-}I}$ (Figure 3C), suggesting that homo-oligomerization of both CARD^{MAVS} and 2CARD$^{RIG\text{-}I}$ cooperates to drive tetramer formation of the fusion construct.

Note that the 42 aa linker between 2CARD$^{RIG\text{-}I}$ and CARD^{MAVS} is long enough (~13 nm, in comparison to 5-nm-long 2CARD) so

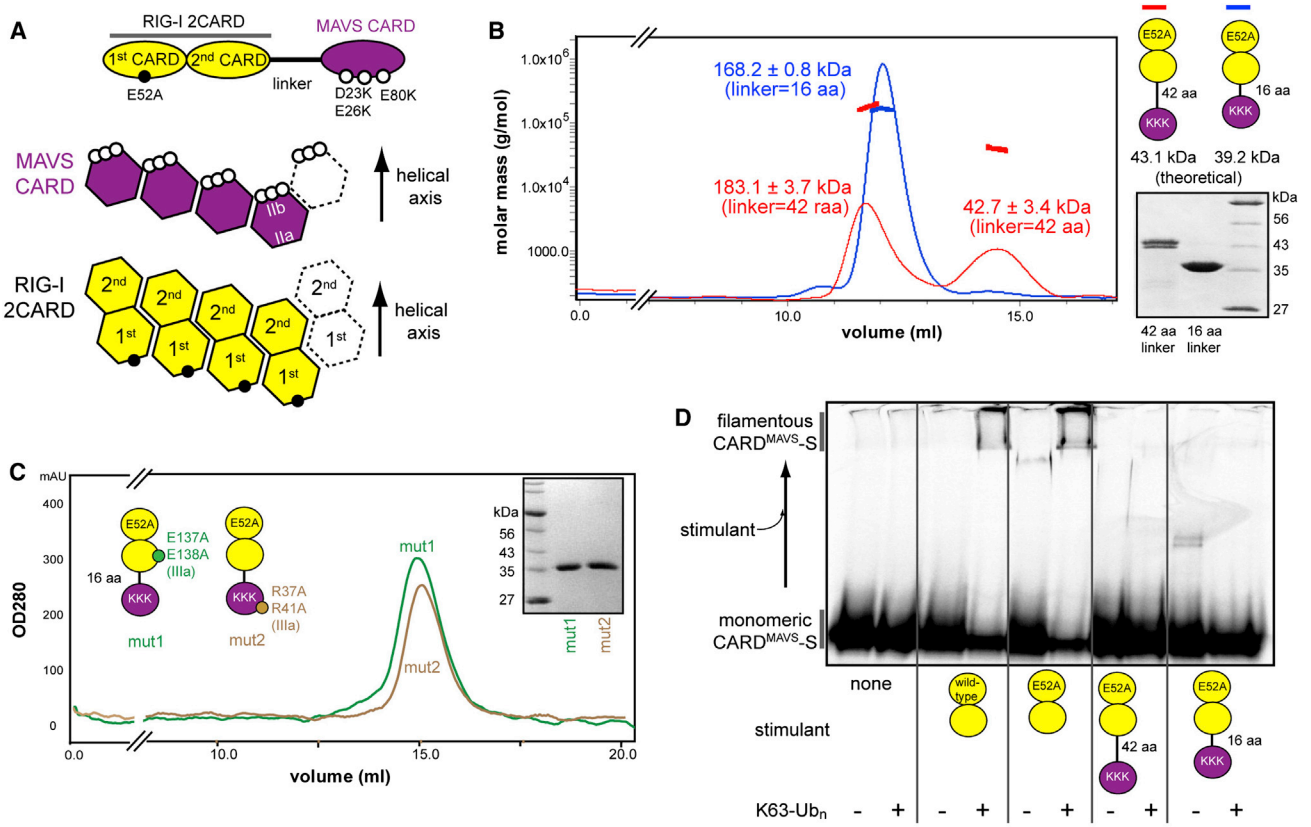

Figure 3. Protein Engineering Strategies for Crystallization of the 2CARD^{RIG-I}:CARD^{MAVS} Complex

(A) 2CARD^{RIG-I} with E52A (filled circle) was fused to CARD^{MAVS} with the triple mutation E23K/E26K/E80K (KKK, open circles). Surface locations of the mutations were indicated in the 2D representation. See Figure S3 for detailed characterization of these mutants.

(B) Analysis of the oligomeric state of the fusion construct in (A) by multiangle light scattering (MALS) coupled to size exclusion chromatography (SEC) using a Superdex200 column. MALS data indicate that the peaks eluted at ~12 ml and ~14.5 ml correspond to the tetramer and monomer, respectively. Shown on the bottom-right corner is the SDS-PAGE analysis (Coomassie stained) of the fusion constructs.

(C) SEC trace of the fusion constructs (16 aa linker) with E137A/E138A (green circle, mut1) on 2CARD^{RIG-I} and R37A/R41A (brown circle, mut2) on CARD^{MAVS}, using a Superdex200 column. Both mut1 and mut2 fusion proteins elute at ~14.5 ml, suggesting that these mutants exist as monomers. Inset: SDS-PAGE analysis of the mut1 and mut2 fusion proteins.

(D) MAVS stimulatory activity of the fusion constructs. Monomer-to-filament transition of fluorescently labeled CARD^{MAVS}-S was monitored by native gel assay. CARD^{MAVS}-S was incubated with wild-type or E52A 2CARD^{RIG-I} or fusion constructs in the presence or absence of K63-Ub$_n$.

that it alone would not impose geometric restraints to the conjugated proteins. Thus, the impact of the 2CARD$^{RIG-I(E52A)}$ fusion on blocking CARD$^{MAVS(KKK)}$ from forming oligomers beyond a tetramer suggests that 2CARD$^{RIG-I(E52A)}$ forms a specific interaction with CARD$^{MAVS(KKK)}$. Consistent with this interpretation, the 2CARD$^{RIG-I(E52A)}$-CARD$^{MAVS(KKK)}$ fusion protein did not stimulate filament formation of wild-type CARD^{MAVS}-S, regardless of the linker length or K63-Ub$_n$ (Figure 3D). This is unlike isolated 2CARD$^{RIG-I(E52A)}$, which robustly stimulates the monomer-to-filament transition of CARD^{MAVS}-S in the presence of K63-Ub$_n$, and suggests that 2CARD$^{RIG-I(E52A)}$ in the fusion construct interacts with CARD$^{MAVS(KKK)}$ using the surface that is otherwise involved in stimulating wild-type CARD^{MAVS}-S.

Our initial effort to crystallize the 2CARD$^{RIG-I(E52A)}$-CARD$^{MAVS(KKK)}$ tetramer with the 16 aa linker produced small crystals. The crystal quality was dramatically improved upon addition of mono-Ub, which did not bind the 2CARD-CARD tetramer in solution, but acted as a crystallographic packing reagent (Figure S4F). The structure was determined by molecular replacement, and refined to 3.4 Å at R_{work} and R_{free} of 19.1% and 23.9%, respectively (Table 2).

Crystal Structure of the 2CARD^{RIG-I}:CARD^{MAVS} Complex

The crystal structure revealed that CARD^{MAVS} is stacked on top of the second CARD^{RIG-I} through IIa:IIb interactions, and that the four copies of the 2CARD-CARD fusion protein form a helical tetramer (Figures 4A and 4B). The electron density map for the linker between 2CARD^{RIG-I} and CARD^{MAVS} was poorly defined, suggesting flexibility in the linker. The identical tetrameric architecture of 2CARD-CARD was observed in two independent copies in the asymmetric unit (Figures S4A and S4B), which supports that the crystal structure represents their native assembly architecture in solution. The two copies of the tetramer in the crystal lattice are stacked bottom to bottom, using the

Table 2. Data Collection and Refinement Statistics of the 2CARD^{RIG-I}:CARD^{MAVS} Complex Structure

	Crystal 1
Data Collection	
Space group	$P2_1\ 2_1\ 2_1$
Cell dimensions	
a, *b*, *c* (Å)	111.8, 117.3, 257.5
α, β, γ (°)	90.0, 90.0, 90.0
Resolution (Å)	46.8–3.4 (3.64–3.40)*
R_{sym} or R_{merge}	0.16 (1.32)
$I/\sigma I$	8.28 (1.26)
Completeness (%)	99.1 (97.8)
Redundancy	3.3 (3.2)
Refinement	
Resolution (Å)	46.8–3.40 (3.44–3.40)
No. reflections	89,450 (3,005)
R_{work}/R_{free}	0.19 (0.32)/0.24 (0.33)
No. atoms	
Protein	43,375
Ligand/ion	
Water	
B factors	
Protein	104.09
Ligand/ion	
Water	
Rmsd	
Bond lengths (Å)	0.011
Bond angles (°)	1.268
Ramachandran plot	
Outliers	0.5%
Allowed	99.5%
Favored	96.3%

*Values in parentheses are for highest-resolution shell.

Ia, IIa, and IIIa surface areas of the first CARD^{RIG-I} (Figure S4A). The functional implication of this stacking is unclear, as the tetramer formation of 2CARD^{RIG-I} is sufficient to stimulate MAVS (Peisley et al., 2014), and mutations of the bottom (IIa) of the first CARD^{RIG-I} have little impact on the signaling activity of RIG-I (Peisley et al., 2014). As expected from the requirement for mono-Ub in crystallization, two or three Ubs occupy previously identified Ub binding sites (Peisley et al., 2014) on each of the 2CARD^{RIG-I} tetramers, and mediate crystallographic contacts with adjacent complexes (Figures S4E and S2F). Here, we limit our discussion to the inter-CARD^{MAVS} or inter-CARD^{RIG-I} interactions, as 2CARD^{RIG-I}:Ub interactions were previously discussed (Peisley et al., 2014).

Comparison of the structure of the 2CARD^{RIG-I} tetramer within the 2CARD^{RIG-I}:CARD^{MAVS} complex and that formed in complex with K63-Ub_2 without CARD^{MAVS} (Peisley et al., 2014) showed that their structures are identical (Figure S5A, bottom panel). Similarly, the CARD^{MAVS} tetramer in the 2CARD^{RIG-I}:CARD^{MAVS} complex also showed little difference from the single helical turn of CARD^{MAVS} in the CARD^{MAVS} filament (Figure S5A, top panel). These observations suggest that the covalent fusion of 2CARD^{RIG-I} and CARD^{MAVS} had little impact on their ability to homo-oligomerize. Interestingly, the two helical axes of the 2CARD^{RIG-I} tetramer and the CARD^{MAVS} tetramer coincide such that the first helical turn of the first CARD^{RIG-I}, which is extended by the second helical turn of the second CARD^{RIG-I}, is further extended by the third helical turn of CARD^{MAVS} without any noticeable discontinuity (Figure 4C). In further support of our notion that a single helical symmetry runs from the bottom-most first CARD^{RIG-I} (chain A in Figure 4A) all the way to the top-most CARD^{MAVS} (chain H in Figure 4A), superposition of the 2CARD^{RIG-I}:CARD^{MAVS} complex onto the three-helical turns of our CARD^{MAVS} filament model showed a remarkable match between the two structures (Figure S5B). Accordingly, the CARD^{MAVS} filament structure can be stacked on top of the 2CARD^{RIG-I}:CARD^{MAVS} complex without introducing any discontinuity in the helical symmetry (Figure 4D). Altogether, these observations are consistent with the model that the 2CARD^{RIG-I} tetramer nucleates the CARD^{MAVS} filament by serving as a helical template that recruits individual CARD^{MAVS} along the extended helical trajectory predefined by 2CARD^{RIG-I} (Figure 4D).

Charge-Complementary Mutations Support the 2CARD^{RIG-I}:CARD^{MAVS} Complex Structure

Examination of the 2CARD^{RIG-I}:CARD^{MAVS} interface shows that surfaces Ia, IIa, and IIIa of CARD^{MAVS} interact with Ib, IIb, and IIIb of the second CARD^{RIG-I}, respectively, using a combination of hydrophobic and electrostatic residues (Figure 5A). This interaction mode between 2CARD^{RIG-I} and CARD^{MAVS} is consistent with our previous data (Peisley et al., 2014), showing that D122 and E178/R179 on the surface IIb of the second CARD^{RIG-I} are crucial for MAVS stimulation, but not for its homotetramerization. To further test whether our structure of the 2CARD^{RIG-I}:CARD^{MAVS} complex indeed recapitulates the functional state of 2CARD^{RIG-I} nucleating the CARD^{MAVS} filament, we have extended the charge-complementary mutation analysis of MAVS in Figure 2 to RIG-I.

Our structures indicate that W56 in CARD^{MAVS} interacts with R43 in CARD^{MAVS} within the filament (Figure 1E) or L140 in 2CARD^{RIG-I} within the 2CARD^{RIG-I}:CARD^{MAVS} complex (Figure 5A). We asked whether W56R in CARD^{MAVS} can interact with a charge-complementary mutant L140D (or L140E) in 2CARD^{RIG-I}, as it did with R43D (or R43E) in CARD^{MAVS} (Figure 2). If so, L140D (or L140E) 2CARD^{RIG-I} would stimulate filament formation of CARD^{MAVS} with the W56R/R43D mutation, but not wild-type CARD^{MAVS}. Purified 2CARD^{RIG-I} with L140D and L140E formed the tetramer as well as wild-type 2CARD^{RIG-I} in the presence of K63-Ub_n (Figure 5B). While L140D and L140E significantly reduced the ability of 2CARD^{RIG-I} to stimulate wild-type CARD^{MAVS} (Figure 5C), they conferred a new ability to stimulate filament formation of W56R/R43D CARD^{MAVS} (Figure 5D). A residual stimulatory activity observed with L140E against wild-type CARD^{MAVS} may reflect the more hydrophobic nature of Glu than Asp due to its longer aliphatic side chain. This result suggests that W56 in CARD^{MAVS} directly interacts with L140 in 2CARD^{RIG-I}, and further supports our structure of the 2CARD^{RIG-I}:CARD^{MAVS} complex.

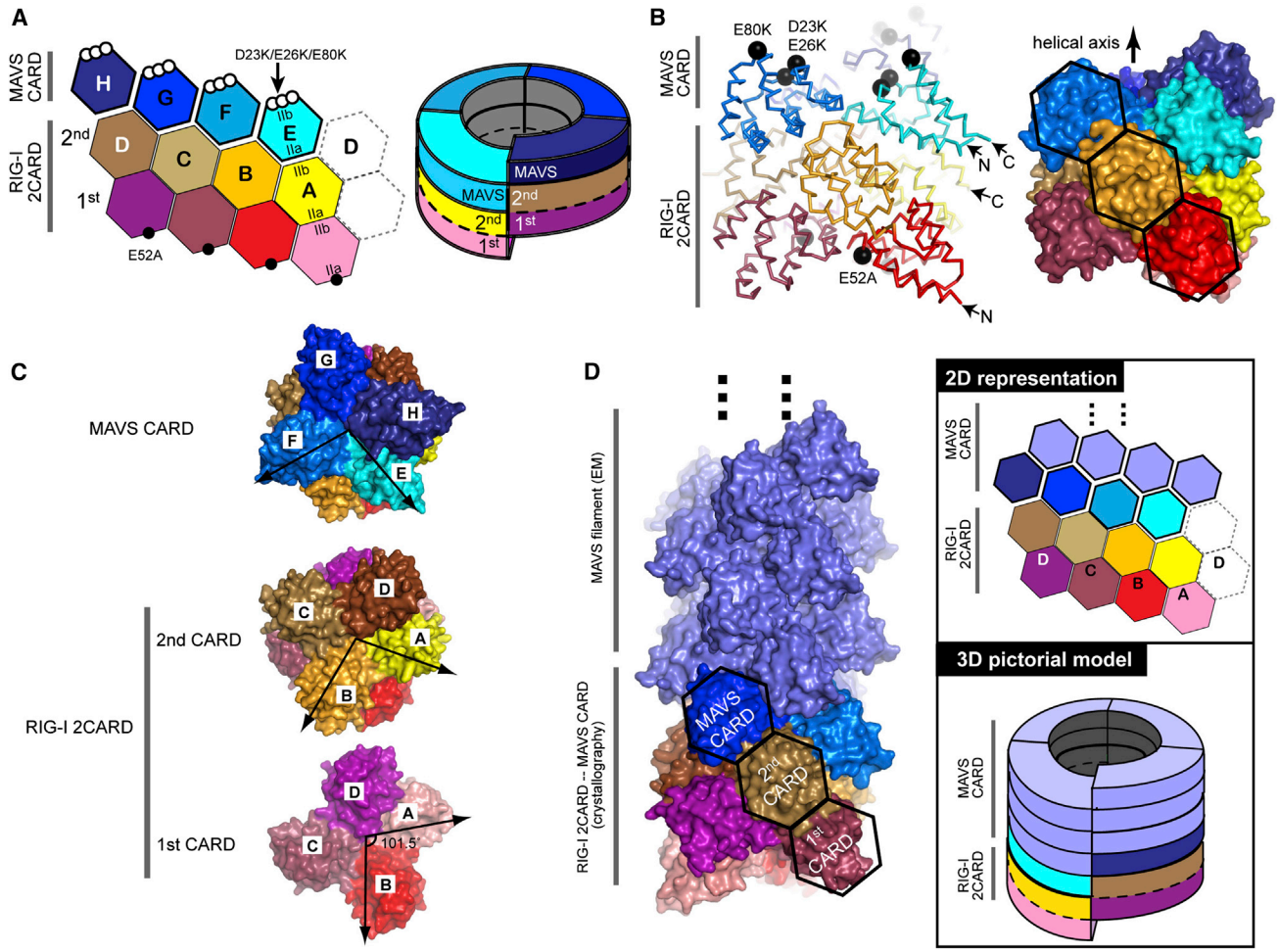

Figure 4. Crystal Structure of the 2CARD^{RIG-I}:CARD^{MAVS} Complex Reveals How the 2CARD^{RIG-I} Tetramer Nucleates the CARD^{MAVS} Filament

(A) 2D representation of the helical architecture of the 2CARD^{RIG-I}:CARD^{MAVS} complex. The mutations E52A and E23K/E26K/E80K are represented by filled and open circles, respectively. On the right is the schematic model of the helical architecture of the complex. The same color code is used throughout Figure 4. See also Figure S4.

(B) Structure of the 2CARD^{RIG-I}:CARD^{MAVS} complex shown in ribbon (left) and surface (right) representations. The N and C termini of 2CARD^{RIG-I} (residues 1 and 188) and CARD^{MAVS} (residues 1 and 97) face the periphery of the helical assembly architecture and are indicated by arrows.

(C) Three helical turns in the 2CARD^{RIG-I}:CARD^{MAVS} complex, looking down the helical axis. The first helical turn formed by the first CARD^{RIG-I} (bottom) is extended by the second helical turn formed by the second CARD^{RIG-I} (middle) and the third helical turn formed by the CARD^{MAVS} (top). The arrows indicate the angular relationship (twist) between the adjacent CARDs.

(D) A model of the CARD^{MAVS} filament nucleated by the 2CARD^{RIG-I} tetramer. The EM structure of the CARD^{MAVS} filament (slate) was stacked on top of the crystal structure of the 2CARD^{RIG-I}:CARD^{MAVS} complex, showing that the helical trajectory of the 2CARD^{RIG-I}:CARD^{MAVS} complex can be further extended to support the CARD^{MAVS} filament propagation. Shown on the right are the 2D (top) and 3D (bottom) schematic models.

Plasticity of the 2CARD^{RIG-I}:CARD^{MAVS} Interface

Comparison of the 2CARD^{RIG-I}:CARD^{MAVS} and CARD^{MAVS}:CARD^{MAVS} interactions shows that the same residues in surfaces Ia, IIa, and IIIa of CARD^{MAVS} interact with Ib, IIb, and IIIb of CARD^{MAVS} within the MAVS filament (Figure 1E) or those of the second CARD^{RIG-I} in the 2CARD:CARD complex (Figure 5A). Sequence comparison between 2CARD^{RIG-I} and CARD^{MAVS} shows that, while CARD^{MAVS} is more homologous to the second CARD^{RIG-I} than to the first CARD^{RIG-I}, residues in Ib–IIIb of the second CARD^{RIG-I} and CARD^{MAVS} are dissimilar (with the exception of D122 in RIG-I, which corresponds to E26 in MAVS) (Figure 6A). These results suggest the plasticity of the CARD^{MAVS} surface, which allows its interaction with at least two distinct combinations of surface residues.

Sequence comparison among RIG-I orthologs shows the lack of strict conservation in the 2CARD^{RIG-I}:CARD^{MAVS} interface (Figure S6A). The sequence divergence is such that none of the residues on the Ib–IIIb surface of human 2CARD^{RIG-I} are preserved in duck. Duck 2CARD^{RIG-I} is inefficient in activating IFNβ signaling pathways in the human cell 293T (Figure 6C), and cannot stimulate filament formation of human MAVS in vitro (Figure 6E). Comparison of the structures of duck and human

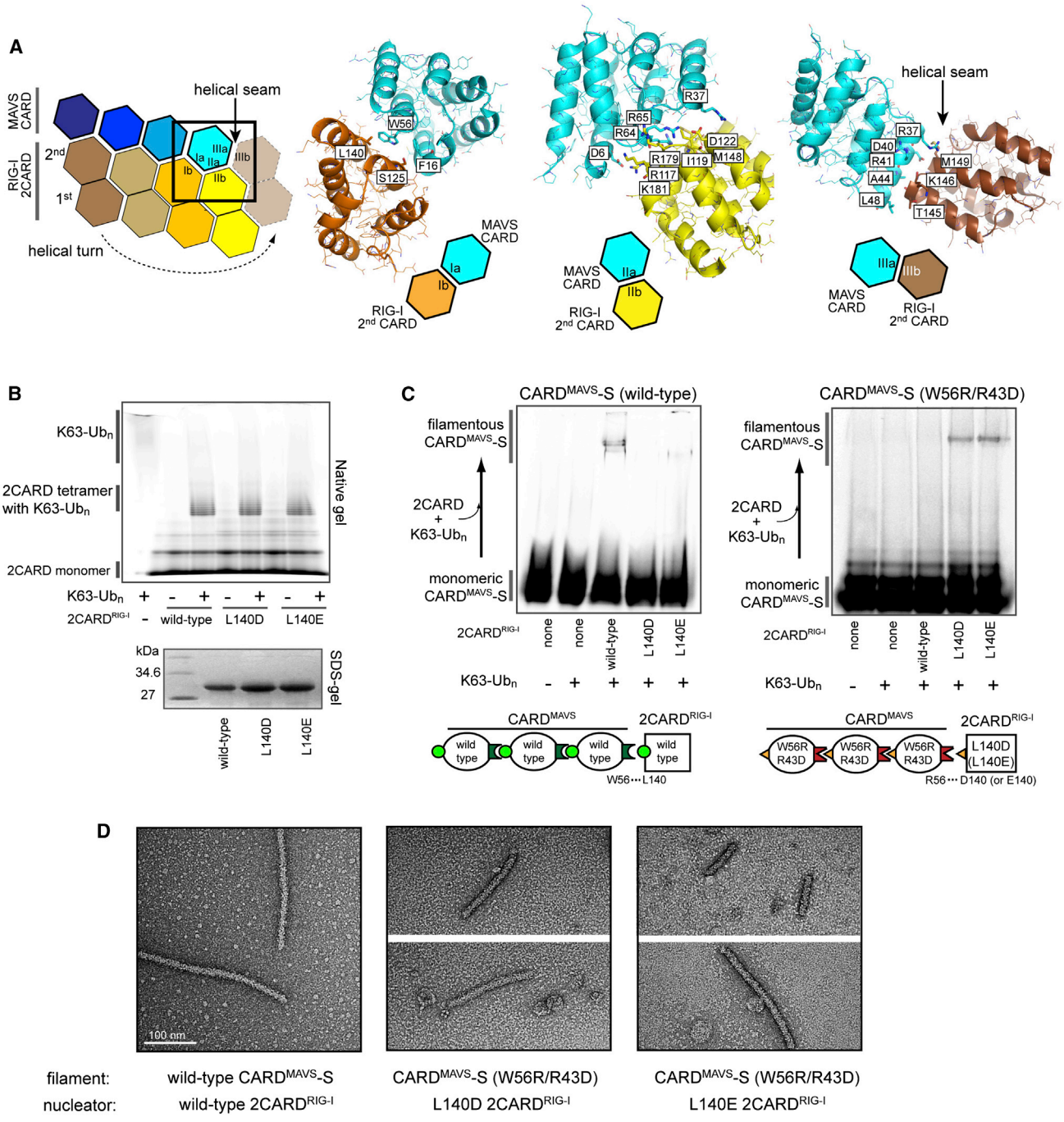

Figure 5. CARD^{MAVS} Interacts with 2CARD^{RIG-I} as It Does with CARD^{MAVS} in the Filament

(A) Details of the 2CARD^{RIG-I}:CARD^{MAVS} interactions. Residues at the interface are shown in stick models. See Figure 1E to compare with the CARD^{MAVS}:CARD^{MAVS} interaction.

(B) Tetramerization of wild-type, L140D, and L140E 2CARD^{RIG-I} in the presence of K63-Ub$_n$, as measured by a native gel analysis. The gel was Krypton-stained.

(C) MAVS stimulatory activity of wild-type and charge-complementary mutant 2CARD^{RIG-I}. Monomer-to-filament transition of wild-type CARD^{MAVS}-S was stimulated by wild-type 2CARD^{RIG-I}, but not by L140D or L140E. Conversely, monomer-to-filament transition of W56R/R43D CARD^{MAVS}-S was stimulated by L140D and L140E 2CARD^{RIG-I}, but not by wild-type 2CARD^{RIG-I}. Shown below are pictorial diagrams that illustrate the effect of charge-complementary mutations.

(D) Representative electron micrographs of the wild-type or W56R/R43D CARD^{MAVS}-S filaments stimulated by wild-type, L140D, or L140E 2CARD^{RIG-I}.

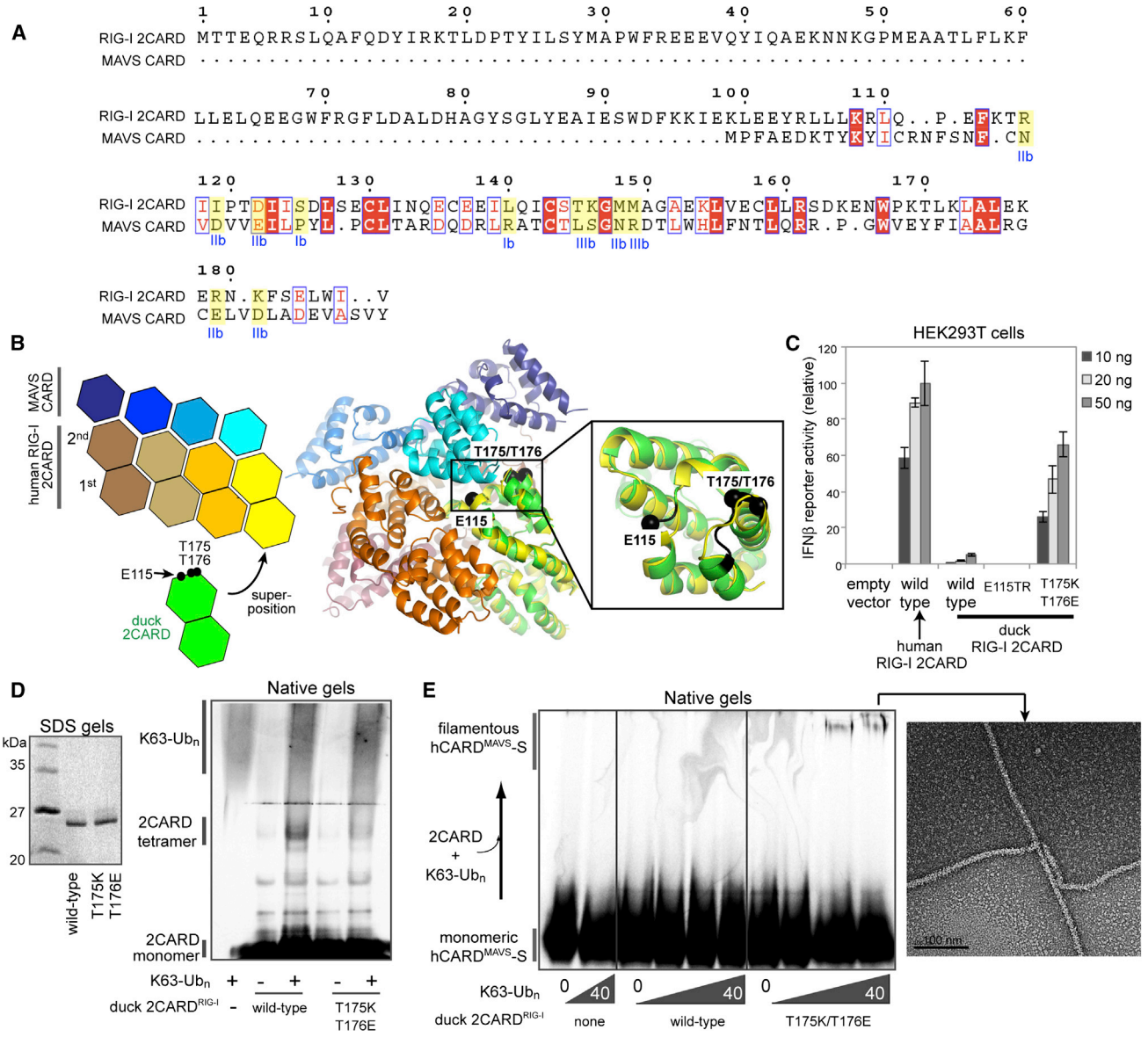

Figure 6. Versatility in Molecular Interface between CARD^{MAVS} and 2CARD^{RIG-I}

(A) Structure-based sequence alignment between 2CARD^{RIG-I} and CARD^{MAVS}. The surface residues interacting with Ia–IIIa of CARD^{MAVS} were highlighted yellow, and the surface types were indicated below (blue).

(B) Superposition of duck 2CARD^{RIG-I} (green, PDB 4A2W) onto human 2CARD^{RIG-I} in the 2CARD^{RIG-I}:CARD^{MAVS} complex. E115 and T175/T176 (black spheres) are located in two loops (colored black on the right) in the 2CARD^{RIG-I}:CARD^{MAVS} interface, which show distinct conformations in human and duck 2CARD^{RIG-I}. See also Figure S6A for sequence comparison.

(C) IFNβ reporter assay of human and duck 2CARD^{RIG-I} in 293T cells (mean ± SD, n = 3). All 2CARDs are N-terminally fused to glutathione S-transferase (GST). See also Figure S6B.

(D) Native gel analysis of tetramerization of wild-type and T175K/T176E 2CARD^{RIG-I} from duck in the presence and absence of K63-Ub$_n$ (Krypton stain). SDS-PAGE analysis (Coomassie stain) is shown on the left.

(E) Human MAVS stimulatory activity of wild-type and T175K/T176E duck 2CARD^{RIG-I}. Monomer-to-filament transition of fluorescently labeled human CARD^{MAVS}-S was monitored in the presence of duck 2CARD^{RIG-I} and increasing concentrations of K63-Ub$_n$. Shown on the right is a representative electron micrograph of the human CARD^{MAVS}-S filaments stimulated by duck 2CARD^{RIG-I} with T175K/T176E.

2CARD^{RIG-I} suggests that, while the overall conformation of 2CARD is well conserved (α root-mean-square deviation [rmsd] of 0.8 Å), two loops in IIb slightly differ in their backbone geometry (Figure 6B). In our effort to understand how human MAVS discriminates between human and duck 2CARD^{RIG-I}, we have mutated E115 and T175/T176 in these loops in duck 2CARD^{RIG-I} to mimic human 2CARD^{RIG-I}. A replacement of E115 by T and insertion of R (E115TR) (as in human RIG-I) did

not increase the signaling activity of duck 2CARD^{RIG-I} in 293T cells. However, replacement of T175/T176 by K175/E176 (as in human RIG-I) increased the signaling activity of duck 2CARD^{RIG-I} in 293T cells to the level comparable to human 2CARD^{RIG-I} (Figure 6C). Consistently, our in vitro assay showed that duck 2CARD^{RIG-I} with T175K/T176E, but not the wild-type, induced filament formation of human CARD^{MAVS} (Figure 6E), while both T175K/T176E and wild-type can form tetramers in the presence of K63-Ub$_n$ (Figure 6D). Interestingly, T175K/T176E in duck RIG-I did not result in a compensatory loss of its signaling activity in chicken cells, DF-1 (Figure S6B), suggesting that the mutation leads to selective increase in its stimulatory activity against human MAVS without affecting its activity against chicken MAVS. Considering that the composition of the residues in the 2CARD:CARD interface remains significantly different between human and duck 2CARD^{RIG-I} even after the T175K/T176E mutation, the newly acquired compatibility between duck 2CARD^{RIG-I} and human CARD^{MAVS} further highlights the remarkable plasticity of the 2CARD:CARD interface.

DISCUSSION

Mechanistic studies of filament nucleation processes often confront multiple challenges, including the difficulty of crystallizing a polymerizing protein and the intrinsic limitation of EM helical reconstruction in analyzing nonrepeating elements, such as the nucleator. In the case of RIG-I and MAVS, the apparently transient interaction between 2CARD^{RIG-I} and CARD^{MAVS} has further defied previous studies to understand how 2CARD^{RIG-I}, in particular its tetrameric form, triggers the CARD^{MAVS} filament formation, the committed step in the IFNβ signaling pathway of RIG-I. The structures of the CARD^{MAVS} filament and the 2CARD^{RIG-I}:CARD^{MAVS} complex reported in this manuscript thus reveal a long-sought-after mechanism of MAVS filament nucleation by RIG-I. We found that the helical tetrameric architecture of 2CARD^{RIG-I} serves as a template that recruits individual CARD^{MAVS} along the extended helical trajectory predefined by the 2CARD^{RIG-I} tetramer (Figure 4D). As a result, the left-handed single-stranded helical architecture of the 2CARD^{RIG-I} tetramer (with a helical pitch of a single CARD) is precisely preserved in the CARD^{MAVS} filament (Figure 1F). As CARD^{MAVS} is recruited to the composite surface on the 2CARD^{RIG-I} tetramer formed by adjacent 2CARD^{RIG-I} subunits, our findings thus explain the requirement for 2CARD tetramerization in MAVS activation and argue against a scenario where individual 2CARD:CARD interactions can stimulate MAVS filament formation. While only the second CARD^{RIG-I} forms a direct contact with MAVS, we have previously shown that the tight intramolecular interaction between the first and second CARDs is required for stable tetramerization of 2CARD^{RIG-I} (Peisley et al., 2014), which explains the observed requirement for both the first and second CARDs for RIG-I to activate downstream signaling pathways (Gack et al., 2008).

A corollary of this nucleation mechanism is that CARD^{MAVS} interacts with 2CARD^{RIG-I} in the same manner as it does with other CARD^{MAVS} in the filament. The divergence between 2CARD^{RIG-I} and CARD^{MAVS} sequences, especially in residues interacting with a common surface on CARDs^{MAVS}, indicates a remarkable plasticity in the CARD-CARD interactions utilized in the RIG-I-MAVS (and presumably MDA5-MAVS, Figures S6C and S6D) signaling pathway. It is possible that the apparently broad specificity reflects the sufficiency of transient (thus weak) interaction between 2CARD^{RIG-I} and CARD^{MAVS} for nucleating the MAVS filament. A transient interaction between 2CARD^{RIG-I} and CARD^{MAVS} may allow a small number of RIG-I molecules to nucleate multiple MAVS filaments, thus amplifying the antiviral signal, while a stable interaction could be restricted to nucleating a single MAVS filament. This raises an intriguing question of whether MAVS stimulation is limited to RIG-I and MDA5, or if there could be other CARD-containing proteins that also stimulate MAVS filament formation. Understanding the precise nature of the CARD-CARD specificity for MAVS activation would require future investigation.

How do our findings on isolated CARD^{MAVS} and 2CARD^{RIG-I} translate to the signaling mechanism of full-length RIG-I/MDA5 and MAVS? We have previously shown that the RNA binding domains (helicase and CTD) of RIG-I and MDA5 form filamentous oligomers along dsRNA and utilize the proximity-induced oligomerization mechanism (as well as the ubiquitin-mediated mechanism for RIG-I) to assemble the 2CARD oligomers alongside the filament (Peisley et al., 2013; Wu et al., 2013) (Figure 7). Consistent with this notion, 2CARD^{RIG-I} in its homotetrameric structure exposes its C terminus to the periphery of the oligomer (Figure 4B), so that the linker (~50 aa) between 2CARD and the helicase domain could tether the 2CARD tetramer to the RIG-I core filament (Figure 7). The 2CARD^{RIG-I} tetramer would then recruit individual MAVS CARDs by extending the helical trajectory of the second CARD^{RIG-I}, nucleating the self-perpetuating filament of CARD^{MAVS} (Figure 7). As with 2CARD^{RIG-I}, the C terminus of CARD^{MAVS} faces outward (Figure 1B), allowing formation of the CARD^{MAVS} filament while being anchored to the mitochondrial outer membrane via the ~400-aa-long linker (Figure 7). Only upon CARD^{MAVS} filament formation can MAVS recruit TRAF molecules and activate the downstream signaling pathway (Hou et al., 2011), consistent with the known preference of TRAFs for oligomerized target proteins (Wu, 2004).

Our findings not only provide unique insights into the signal activation mechanism of RIG-I and MAVS, but also implicate a mechanism that could be potentially applicable to a broad range of innate immune receptors. These include AIM2 and NLRP3 in inflammasomes, which together with RIG-I are emerging as a new class of receptors that activate downstream immune response via filament nucleation of their respective adaptor molecules (Cai et al., 2014; Lu et al., 2014). Furthermore, the crystallization strategies developed in this work offer a generalizable methodology to investigate filament nucleation mechanisms of other receptors.

EXPERIMENTAL PROCEDURES

Detailed experimental procedures are provided in Supplemental Information.

Cryo-EM and Helical Reconstruction of the MAVS CARD Filament

Human CARD^{MAVS} with an N-terminal 19 aa extension and P2A were purified in buffer A (20 mM HEPES [pH 7.5], 150 mM NaCl) as described in Figure S1C. For cryo-EM, 3.5 μl of the CARD^{MAVS} filament sample (0.2 mg/ml) was applied to glow-discharged Quantifoil R1.2/1.3 holy carbon grids (Quantifoil, Germany)

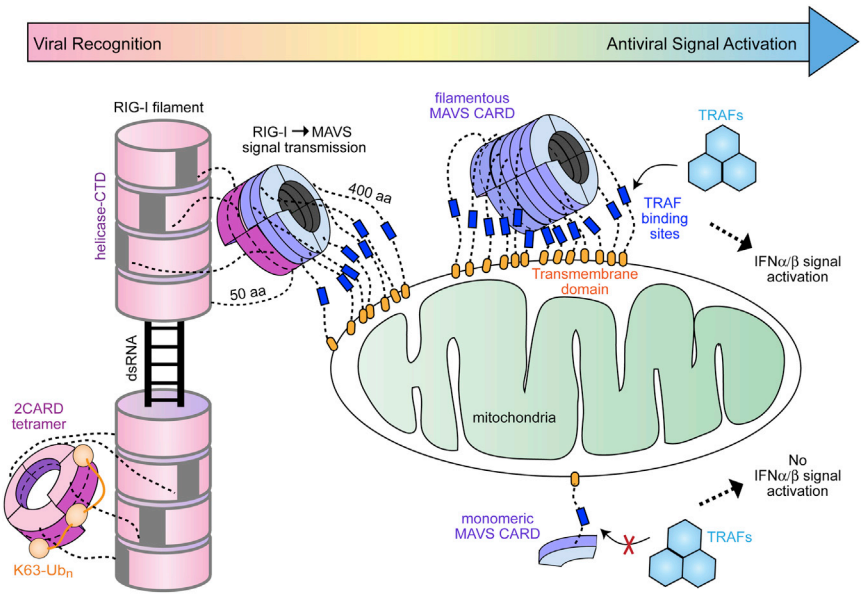

Figure 7. A Model of Signal Activation by Full-Length RIG-I and MAVS

Upon encountering viral dsRNA with 5′ppp and blunt end, the RNA binding domain (helicase-CTD) of RIG-I forms filamentous oligomers along the length of dsRNA in an ATP-dependent manner (Peisley et al., 2013). This filament formation brings together 2CARDs into proximity, and induces tetramerization of 2CARD while being tethered to the core filament via a 50 aa flexible linker (Peisley et al., 2013). Tetramerization of 2CARD may also be induced by K63-Ub$_n$, which stabilizes the 2CARD tetramer by bridging between adjacent 2CARDs and wrapping around the tetramer (Peisley et al., 2014). The 2CARD tetramer resembles the lock-washer (helical ring) structure, which serves as a helical template that nucleates the MAVS CARD filament. MAVS CARD is anchored to the mitochondrial outer membrane via a ~400-aa-long linker, which contains the TRAF binding sites. Filament formation of MAVS CARD would bring together multiple TRAF binding sites into proximity, which appears to be important for efficient recruitment of TRAF molecules and activation of further downstream signaling pathways (Hou et al., 2011; Takamatsu et al., 2013).

and plunge-frozen using a Vitrobot Mark I (FEI). Data collection was performed on a Tecnai F20 electron microscope (FEI) operated at an acceleration voltage of 200 kV using a CT3500 cryo-specimen holder (Gatan) and the UCSF Image4 software (Li et al., 2013).

The SPARX software suite (Hohn et al., 2007) was used for all steps of image processing. Initially, we windowed segments 256 × 256 pixels with 75 pixels translation between them, yielding 12,817 segments. The average power spectrum showed an unambiguous layer lines pattern with a meridional reflection at 1/5.13 Å^{-1}. Thus, the axial rise per asymmetric unit in the filament was 5.13 Å (Figure S1D). Indexing of the layer lines yielded an azimuthal rotation per subunit of 101.1þ (Figure S1D). The helical reconstruction was performed using Helicon in SPARX. Using the established helical symmetry parameters, the segments were automatically windowed from filaments using segment size of 256 × 256 pixels and a 5 pixel gap between each segment. First, we performed five iterations of the ab initio structure determination, which converged rapidly, yielding a filament structure in which individual subunits unmistakably resembled the structure of the monomeric MAVS CARD (Potter et al., 2008). Therefore, we proceeded with 20 iterations of local refinement, during which geometric constraints from the helical symmetry were progressively relaxed and out-of-plane tilts (range 80°–100°) were allowed. The resolution (3.6 Å) was estimated using the FSC = 0.5 criterion.

To create a model of the two helical turns of the CARD^{MAVS} filament, eight copies of CARD^{MAVS} were docked into the density map using the program Coot (Emsley and Cowtan, 2004). The density map was cropped to just cover the modeled portion of the filament (within 3 Å) using the phenix.cut_out_density command in the program Phenix (Adams et al., 2010). For refinement, phenix.refine was used with an arbitrary space group and unit cell dimensions. A summary of structure refinement statistics is provided in Table 1.

Crystallization and Structure Determination of the 2CARD$^{RIG\text{-}I}$:CARD^{MAVS} Complex

The 2CARD$^{RIG\text{-}I}$-CARD^{MAVS} fusion construct was expressed in BL21(DE3) at 20þC for 16–20 hr following induction with 0.4 mM IPTG, and was purified by Ni-NTA affinity chromatography. The 6xHis tag was removed by HRV 3C protease, and 2CARD was further purified by additional Ni-NTA affinity chromatography and size exclusion chromatography (SEC) in buffer A. The tetrameric species were isolated from SEC, mixed with mono-Ub at a molar ratio of 2:1 (fusion construct:Ub), and concentrated to ~10 mg/ml in buffer A with 2 mM dithiothreitol (DTT). Crystals were obtained as small rods using the hanging-drop vapor-diffusion method from a 1:1 mixture of sample and reservoir buffer that contained 0.22 M Tri-Li Citrate, 18% PEG3350, and 10 mM Cr(III)Cl$_3$. The crystals were cryo-protected in the reservoir buffer containing 15%–20% ethylene glycol for 5 min prior to flash freezing in liquid nitrogen. Diffraction data were collected at beamline 21ID-F (LS-CAT) at the Advanced Photon Source and processed using the program XDS (Kabsch, 2010). The structure was determined by molecular replacement using Phaser (McCoy et al., 2007) and refined using Phenix (Adams et al., 2010) (see Supplemental Information). A summary of data collection and structure refinement statistics is provided in Table 2.

ACCESSION NUMBERS

The atomic models and the cryo-EM densities of the MAVS CARD filament were deposited with accession codes PDB 3J6J and EMD 5922, respectively. The Protein Data Bank (PDB) accession code for coordinates and structure factors for the 2CARD$^{RIG\text{-}I}$:CARD^{MAVS} complex is 4P4H.

SUPPLEMENTAL INFORMATION

Supplemental Information includes six figures, one table, and Supplemental Experimental Procedures and can be found with this article online at http://dx.doi.org/10.1016/j.molcel.2014.06.010.

ACKNOWLEDGMENTS

The authors acknowledge the Texas Advanced Computing Center (TACC) at The University of Texas at Austin for providing high-performance computing resources. B.W. acknowledges the Charles King Postdoctoral Fellowship. E.H.E. acknowledges EB001567. K.E.M. acknowledges CIHR MOP 125865. T.W. is an Investigator in the Howard Hughes Medical Institute. P.A.P. acknowledges GM U54 094598 and GM R01 60635. S.H. acknowledges the Pew Scholarship and BCH Career Development Award.

Received: April 9, 2014
Revised: May 12, 2014
Accepted: June 2, 2014
Published: July 10, 2014

REFERENCES

Adams, P.D., Afonine, P.V., Bunkóczi, G., Chen, V.B., Davis, I.W., Echols, N., Headd, J.J., Hung, L.-W., Kapral, G.J., Grosse-Kunstleve, R.W., et al. (2010). PHENIX: a comprehensive Python-based system for macromolecular structure solution. Acta Crystallogr. D Biol. Crystallogr. *66*, 213–221.

Berke, I.C., Yu, X., Modis, Y., and Egelman, E.H. (2012). MDA5 assembles into a polar helical filament on dsRNA. Proc. Natl. Acad. Sci. USA *109*, 18437–18441.

Berke, I.C., Li, Y., and Modis, Y. (2013). Structural basis of innate immune recognition of viral RNA. Cell. Microbiol. *15*, 386–394.

Cai, X., Chen, J., Xu, H., Liu, S., Jiang, Q.-X., Halfmann, R., and Chen, Z.J. (2014). Prion-like polymerization underlies signal transduction in antiviral immune defense and inflammasome activation. Cell *156*, 1207–1222.

Egelman, E.H. (2010). Reconstruction of helical filaments and tubes. Methods Enzymol. *482*, 167–183.

Emsley, P., and Cowtan, K. (2004). Coot: model-building tools for molecular graphics. Acta Crystallogr. D Biol. Crystallogr. *60*, 2126–2132.

Ferrao, R., and Wu, H. (2012). Helical assembly in the death domain (DD) superfamily. Curr. Opin. Struct. Biol. *22*, 241–247.

Gack, M.U., Kirchhofer, A., Shin, Y.C., Inn, K.S., Liang, C., Cui, S., Myong, S., Ha, T., Hopfner, K.P., and Jung, J.U. (2008). Roles of RIG-I N-terminal tandem CARD and splice variant in TRIM25-mediated antiviral signal transduction. Proc. Natl. Acad. Sci. USA *105*, 16743–16748.

Hohn, M., Tang, G., Goodyear, G., Baldwin, P.R., Huang, Z., Penczek, P.A., Yang, C., Glaeser, R.M., Adams, P.D., and Ludtke, S.J. (2007). SPARX, a new environment for Cryo-EM image processing. J. Struct. Biol. *157*, 47–55.

Hou, F., Sun, L., Zheng, H., Skaug, B., Jiang, Q.X., and Chen, Z.J. (2011). MAVS forms functional prion-like aggregates to activate and propagate antiviral innate immune response. Cell *146*, 448–461.

Jiang, F., Ramanathan, A., Miller, M.T., Tang, G.-Q., Gale, M., Jr., Patel, S.S., and Marcotrigiano, J. (2011). Structural basis of RNA recognition and activation by innate immune receptor RIG-I. Nature *479*, 423–427.

Jiang, X., Kinch, L.N., Brautigam, C.A., Chen, X., Du, F., Grishin, N.V., and Chen, Z.J. (2012). Ubiquitin-induced oligomerization of the RNA sensors RIG-I and MDA5 activates antiviral innate immune response. Immunity *36*, 959–973.

Kabsch, W. (2010). XDS. Acta Crystallogr. D Biol. Crystallogr. *66*, 125–132.

Kato, H., Takeuchi, O., Mikamo-Satoh, E., Hirai, R., Kawai, T., Matsushita, K., Hiiragi, A., Dermody, T.S., Fujita, T., and Akira, S. (2008). Length-dependent recognition of double-stranded ribonucleic acids by retinoic acid-inducible gene-I and melanoma differentiation-associated gene 5. J. Exp. Med. *205*, 1601–1610.

Kato, H., Takahasi, K., and Fujita, T. (2011). RIG-I-like receptors: cytoplasmic sensors for non-self RNA. Immunol. Rev. *243*, 91–98.

Kowalinski, E., Lunardi, T., McCarthy, A.A., Louber, J., Brunel, J., Grigorov, B., Gerlier, D., and Cusack, S. (2011). Structural basis for the activation of innate immune pattern-recognition receptor RIG-I by viral RNA. Cell *147*, 423–435.

Li, X., Mooney, P., Zheng, S., Booth, C.R., Braunfeld, M.B., Gubbens, S., Agard, D.A., and Cheng, Y. (2013). Electron counting and beam-induced motion correction enable near-atomic-resolution single-particle cryo-EM. Nat. Methods *10*, 584–590.

Liu, S., Chen, J., Cai, X., Wu, J., Chen, X., Wu, Y.-T., Sun, L., and Chen, Z.J. (2013). MAVS recruits multiple ubiquitin E3 ligases to activate antiviral signaling cascades. eLife *2*, e00785.

Lu, A., Magupalli, V.G., Ruan, J., Yin, Q., Atianand, M.K., Vos, M.R., Schröder, G.F., Fitzgerald, K.A., Wu, H., and Egelman, E.H. (2014). Unified polymerization mechanism for the assembly of ASC-dependent inflammasomes. Cell *156*, 1193–1206.

Luo, D., Ding, S.C., Vela, A., Kohlway, A., Lindenbach, B.D., and Pyle, A.M. (2011). Structural insights into RNA recognition by RIG-I. Cell *147*, 409–422.

McCoy, A.J., Grosse-Kunstleve, R.W., Adams, P.D., Winn, M.D., Storoni, L.C., and Read, R.J. (2007). Phaser crystallographic software. J. Appl. Cryst. *40*, 658–674.

Patel, J.R., Jain, A., Chou, Y.Y., Baum, A., Ha, T., and García-Sastre, A. (2013). ATPase-driven oligomerization of RIG-I on RNA allows optimal activation of type-I interferon. EMBO Rep. *14*, 780–787.

Peisley, A., Lin, C., Wu, B., Orme-Johnson, M., Liu, M., Walz, T., and Hur, S. (2011). Cooperative assembly and dynamic disassembly of MDA5 filaments for viral dsRNA recognition. Proc. Natl. Acad. Sci. USA *108*, 21010–21015.

Peisley, A., Jo, M.H., Lin, C., Wu, B., Orme-Johnson, M., Walz, T., Hohng, S., and Hur, S. (2012). Kinetic mechanism for viral dsRNA length discrimination by MDA5 filaments. Proc. Natl. Acad. Sci. USA *109*, E3340–E3349.

Peisley, A., Wu, B., Yao, H., Walz, T., and Hur, S. (2013). RIG-I forms signaling-competent filaments in an ATP-dependent, ubiquitin-independent manner. Mol. Cell *51*, 573–583.

Peisley, A., Wu, B., Xu, H., Chen, Z.J., and Hur, S. (2014). Structural basis for ubiquitin-mediated antiviral signal activation by RIG-I. Nature *509*, 110–114.

Pichlmair, A., and Reis e Sousa, C. (2007). Innate recognition of viruses. Immunity *27*, 370–383.

Potter, J.A., Randall, R.E., and Taylor, G.L. (2008). Crystal structure of human IPS-1/MAVS/VISA/Cardif caspase activation recruitment domain. BMC Struct. Biol. *8*, 11.

Rawling, D.C., and Pyle, A.M. (2014). Parts, assembly and operation of the RIG-I family of motors. Curr. Opin. Struct. Biol. *25C*, 25–33.

Takamatsu, S., Onoguchi, K., Onomoto, K., Narita, R., Takahasi, K., Ishidate, F., Fujiwara, T.K., Yoneyama, M., Kato, H., and Fujita, T. (2013). Functional characterization of domains of IPS-1 using an inducible oligomerization system. PLoS ONE *8*, e53578.

Takeuchi, O., and Akira, S. (2009). Innate immunity to virus infection. Immunol. Rev. *227*, 75–86.

Wilkins, C., and Gale, M., Jr. (2010). Recognition of viruses by cytoplasmic sensors. Curr. Opin. Immunol. *22*, 41–47.

Wu, H. (2004). Assembly of post-receptor signaling complexes for the tumor necrosis factor receptor superfamily. Adv. Protein Chem. *68*, 225–279.

Wu, B., Peisley, A., Richards, C., Yao, H., Zeng, X., Lin, C., Chu, F., Walz, T., and Hur, S. (2013). Structural basis for dsRNA recognition, filament formation, and antiviral signal activation by MDA5. Cell *152*, 276–289.

Xu, H., He, X., Zheng, H., Huang, L.J., Hou, F., Yu, Z., de la Cruz, M.J., Borkowski, B., Zhang, X., Chen, Z.J., et al. (2014). Structural basis for the prion-like MAVS filaments in antiviral innate immunity. eLife *3*, e01489.

Yoneyama, M., and Fujita, T. (2008). Structural mechanism of RNA recognition by the RIG-I-like receptors. Immunity *29*, 178–181.